New insights into the interface characteristics of a duplex stainless steel subjected to accelerated ferrite-to-austenite transformation

N. Haghdadi[1,2,*] , P. Cizek[1], P. D. Hodgson[1], Y. He[3], B. Sun[4], J. J. Jonas[5], G. S. Rohrer[6], and H. Beladi[1]

[1] Institute for Frontier Materials, Deakin University, Waurn Ponds, VIC 3216, Australia

[2] School of Materials Science and Engineering, UNSW Sydney, Kensington, NSW 2052, Australia

[3] CanmetMATERIALS, Natural Resources Canada, Hamilton, ON L8P 0A5, Canada

[4] Max-Planck-Institut für Eisenforschung GmbH, Max-Planck-Straße 1, 40237 Düsseldorf, Germany

[5] Materials Engineering, McGill University, Montreal, QC H3A 0C5, Canada

[6] Department of Materials Science and Engineering, Carnegie Mellon University, Pittsburgh, PA 15213-3890, USA

ABSTRACT

The ferrite-to-austenite phase transformation during water quenching of a duplex stainless steel was studied, where a duplex stainless steel was heated to 1370 °C (delta ferrite region) and quenched to room temperature. The microstructure consisted of coarse ferrite grains and fine needle-like austenite particles. The phase transformation mechanism appeared to be "diffusion-limited" displacive where shear was dominant, but also accompanied by prior or simultaneous diffusional elemental redistribution. A small fraction of the interfaces followed Kurdjumov–Sachs and Nishiyama–Wassermann orientation relationships (ORs) where austenite/ferrite interfaces terminated on $\{111\}_A//\{110\}_F$ planes. The high undercooling associated with the fast cooling rates resulted in a considerable deviation from rational ORs. This was mostly due to the formation of intragranular austenite on Cr_2N particles, which most likely caused a random OR with respect to the ferrite matrix. A detailed transmission electron microscopy (TEM) analysis revealed that the planar interphase boundaries characterised by the rational ORs typically contained one dominant set of parallel, regularly spaced dislocations. TEM analysis also showed the occurrence of small protrusions appearing on the edge/face of some austenite particles. Some of these did not leave a sub-boundary behind and formed a finger-like austenite morphology resulting from the instability mechanism. In some other cases, the protruded austenite possessed a low-angle grain boundary with the substrate austenite grain, which was the result of sympathetic nucleation of austenite on a pre-existing austenite particle.

Address correspondence to E-mail: nima.haghdadi@unsw.edu.au

🙛 Springer

Introduction

The character, population and spatial distribution of grain boundaries and interfaces is a critical factor determining the physical and mechanical properties of polycrystalline materials [1–3]. A detailed and statistically meaningful description of the structures of these interfaces, therefore, plays a vital role in understanding the behaviour of these materials. The phase transformation path is one of the most common parameters affecting the character of grain boundaries and interphase boundaries [4, 5]. This is particularly important in the case of steels as they undergo two different solid-state phase transformations upon cooling including the delta ferrite-to-austenite and subsequently the austenite–to-ferrite/bainite/martensite transition. While a considerable amount of work has been carried out on the austenite (face-centred cubic, FCC)-to-ferrite/bainite/martensite (body-centred cubic, BCC or body-centred tetragonal, BCT) transformation, the reverse phase transformation (i.e., BCC to FCC) has received less attention. Duplex stainless steels are excellent model alloys to study the ferrite-to-austenite phase transformation due to the considerable expansion of the delta ferrite region in the phase diagram of this steel.

Duplex stainless steels offer a wide range of attractive properties such as high strength, good ductility and excellent corrosion resistance; because of this, they are extensively used in many industries including oil, petro-chemical, construction and marine [6]. In an equilibrium state at room temperature, these steels consist of a duplex microstructure comprising austenite and ferrite. These steels are, in general, solidified as delta ferrite (BCC), which partially transforms to austenite (FCC) on cooling. It has been shown that the cooling rate from the fully ferritic region plays a critical role in adjusting the volume fraction, interphase boundaries characteristics and morphology of austenite [7]. These differences affect the properties of duplex stainless steels such as precipitation tendency [8], impact toughness [9], corrosion resistance [10], hot deformation [11] and superplasticity [12].

It has been shown that the phase transformation during water quenching of delta ferrite exhibits differences as compared to the austenite-to-martensite transformation during water quenching of low carbon steels, as well as the BCC–FCC transformations in Ni–Cr and Cu–Cr alloy systems. In this context,

Qiu and Zhang [13] and Jiao et al. [14] reported that neither facets nor the long axis of rod-shaped austenite precipitates are similar to those of the precipitates in Ni–Cr and Cu–Cr systems although the lattice parameter ratio of duplex stainless steels is similar to those of the Cu–Cr and Ni–Cr systems. Ameyama et al. [15] have also studied the lath-shaped austenite precipitates formed during water quenching of delta ferrite. They reported an interface with features similar to that of the Ni-Cr system, while the long axis of the rod-shaped precipitates significantly deviated from the conjugate plane associated with the Kurdjumov–Sachs orientation relationship. While these works have provided a detailed analysis of the shape and the interface of the austenite particles formed during quenching of duplex stainless steel, they are based on TEM analysis and therefore limited to a few interfaces. A statistically significant study of the interphase boundaries between the austenite and ferrite in these microstructures through complementary methods, e.g. automated electron backscatter diffraction (EBSD), is, therefore, of particular interest.

In order to comprehensively characterize the interface between austenite and ferrite, five independent parameters are needed: three describing the lattice misorientation (usually expressed as a misorientation angle/axis pair) and two parameters specifying the boundary plane orientation. Conventional EBSD provides four out of five macroscopic parameters for full representation of a boundary, but a three-dimensional analysis of the interphase boundaries is needed to extract the plane orientation. The plane orientations can be measured by 3D EBSD, although the complexity and spatial resolution of the technique present challenges, especially for phases with small lateral dimensions. In this work, we have used a relatively new stereological approach that can determine all five independent interphase boundary parameters using conventional EBSD data [16]. This method is coupled with texture and TEM analysis in the current work to provide new insights into the accelerated ferrite-to-austenite phase transformation in duplex stainless steels that have been water quenched from the ferrite region.

Experimental

The experimental material was a duplex stainless steel ($\sim$ 50–50% ferrite/austenite in the hot-rolled condition) with a chemical composition of 0.036 C, 0.321 Si, 1.82 Mn, 0.013 P, 23.2 Cr, 2.90 Mo, 5.6 Ni, 0.034 Co, 0.153 Cu, 0.245 N and remainder Fe (in wt%). The initial hot-rolled plate of the steel was 20 mm in thickness and the microstructure consisted of pancaked austenite and ferrite grains. Small pieces with a size of $\sim$ 10 $\times$ 10 $\times$ 10 mm^3 were cut and reheated to 1370 °C in a muffle furnace, which was purged with argon gas. The samples were isothermally held for 40 min at this temperature to allow the transformation of austenite to ferrite, ending up in a fully ferritic microstructure. The specimens were then water quenched immediately. This heat treatment did not retain the fully ferritic microstructure; fine austenite particles appeared at both the ferrite–ferrite boundaries and inside the ferrite grains.

The overall crystallographic textures of the hot-rolled and heat-treated materials were measured under a field emission gun Quanta 3-D FEI scanning electron microscope (SEM) equipped with a TSL (TexSEM Laboratories, Inc.) detector. The EBSD scans were performed using an accelerating voltage of 20 kV and a working distance of $\sim$ 12 mm. To ensure unbiased and statistically reliable texture analysis, the EBSD measurements were carried out on more than 15 different sample sections for both microstructures. The inverse pole figures for both phases (ferrite and austenite) were then plotted for each microstructure in TSL software, considering an orthorhombic sample symmetry. Transmission electron microscopy (TEM) analysis of thin foils was carried out using a JEOL JEM 2100F microscope at 200 kV. Convergent-beam Kikuchi patterns were used to obtain local crystallographic orientations and misorientations. Energy-dispersive X-ray spectroscopy (EDS) was used to measure the austenite and ferrite chemical compositions for different microstructures in the scanning-transmission electron microscopy (STEM) mode.

Extensive EBSD analysis was carried out to characterize the interfaces/boundaries within the microstructure. The EBSD measurements were performed on the rolling direction–normal direction (RD–ND) section of the specimens with respect to the initial hot-rolled plate. The details about the method used for the specimen preparation for EBSD have

been given elsewhere [17]. A hexagonal grid was used for the data acquisition with a step size of 0.15 μm. To avoid texture-biased results, the EBSD measurements were carried out on several ferrite grains. The average confidence index for each EBSD map was higher than 0.70. For the grain boundary plane analysis, following post-processing routines were carried out on the collected EBSD maps: (1) an iterative grain dilation cleaning with a minimum of 5 pixels grain size, (2) assignment of a single average orientation to each individual grain using 5° of tolerance angle and (3) dividing curved grain boundaries connecting two triple points into linear segments with a boundary deviation limit of 2 pixels (i.e., 0.3 μm). The details of the latter procedure have been given in [18].

In a 2D EBSD, the intersection of a boundary plane with the sample surface appears as a boundary trace. Knowing the crystal orientation on either side of the boundary, the trace can be imported to the bicrystal stereographic projection. For any trace, the corresponding plane would be one of the infinite number of the planes whose normals lie perpendicular to the trace line segment. Such plane normals would comprise a great circle perpendicular to the trace line segment in the stereographic projection. Once these great circles are constructed for multiple segments, e.g. with the same misorientations, they will coincide for a specific plane if there is a unique correct habit plane for that misorientation. Concurrently, the random (incorrect) planes are observed less frequently and can therefore be eradicated with a background subtraction. The boundary character distribution is then fully characterized by a lattice misorientation and a boundary plane orientation. The quantity of the latter is usually measured in multiples of a random distribution (MRD), where an MRD higher than one means such plane is observed more frequently than expected in a random distribution.

In this study, due to the duplex nature of the microstructure, the reconstructed boundaries were classified into three categories, including delta ferrite/delta ferrite interface, delta ferrite/austenite interphase boundaries and austenite/austenite interface. The numbers of segments collected for these interfaces were 6394, 42457 and 6069, respectively. Plane character distribution analysis was carried out for each of these categories separately, although the focus of the current study is on the ferrite/austenite interphase boundaries.

Results

Initial microstructure

The initial microstructure of the material consisted of both ferrite and austenite grains pancaked along the rolling direction (Fig. 1a). A large number of austenite–austenite boundaries were of a 60°/<111> misorientation angle/axis character representing Σ3 boundaries (Fig. 1a). At the intersection of two Σ3 boundaries, a Σ9 boundary is formed with a 38.9°/<110> misorientation character. These features are confirmed by the misorientation angle distribution (Fig. 1c), which has a very sharp maximum at 60° with a <111> corresponding axis and a secondary local maximum at 39° with a <110> axis (the distributions of these axes are shown in Fig. 3a and b later). Inverse pole figure analysis (Fig. 1b) revealed that the ferrite has a relatively strong <001>//ND texture (intensity ∼ 3.0), while the austenite shows a weak <110>//ND texture (intensity ∼ 1.4). Both the ferrite and austenite textures are similar to the textures previously reported for ferrite and austenite subjected to hot rolling [19, 20].
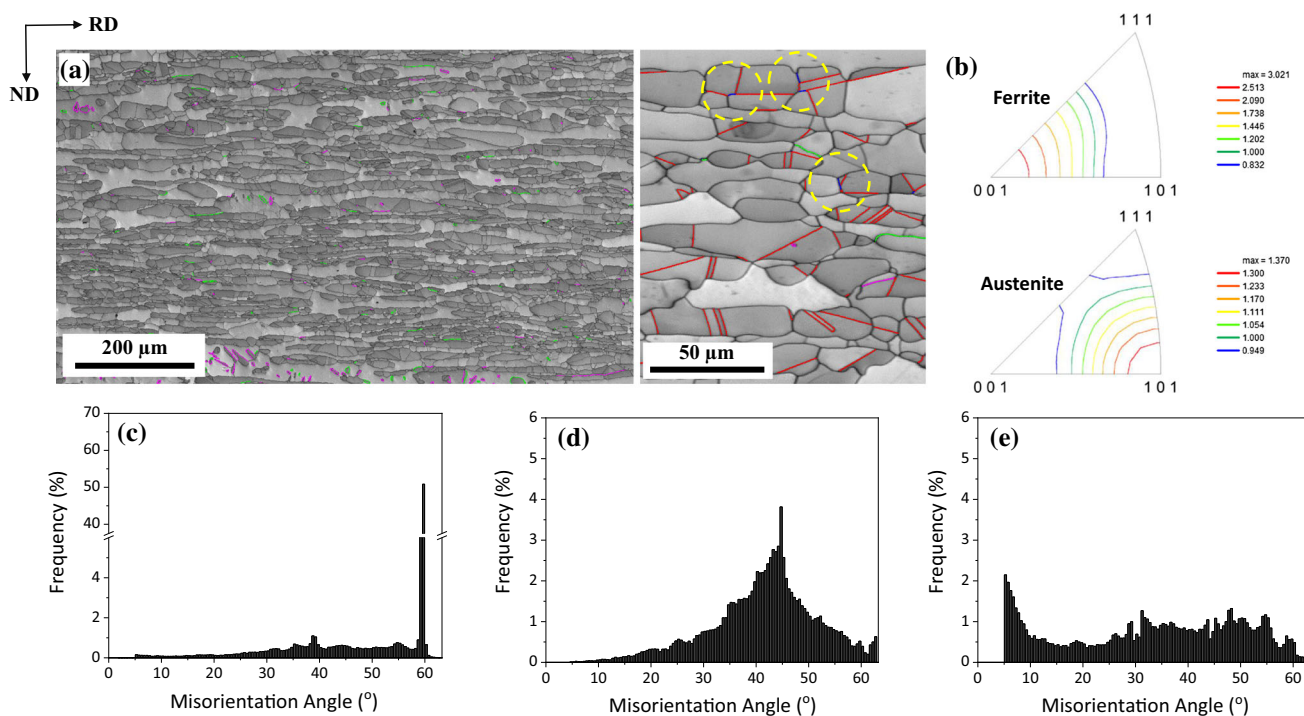
For the austenite–ferrite interfaces, a misorientation peak was noticed around 42°–46° (Fig. 1d), which fell into the same range of misorientations as for the well-known orientation relationships (ORs) between FCC and BCC phases, e.g. Kurdjumov–Sachs (K–S) [21], Nishiyama–Wassermann (N–W) [22], Greninger–Troiano (G–T) [23], Bain [24] and Pitsch [25], see Table 1. However, it was found that only about 2% of the interfaces were of the K–S type, and only about 1% were N–W. The misorientation angle distribution of the ferrite–ferrite boundaries did not show apparent specific peaks and was relatively uniform, except for a local maximum at small misorientation angles (Fig. 1e).

Microstructure characteristics after heat treatment

EBSD analysis

The microstructure of the alloy after heat treatment consisted of coarse ferrite grains and fine needle-like austenite particles (Fig. 2a), suggesting that the austenite particles were most likely precipitated on

Figure 1 Characteristics of the starting hot-rolled steel obtained by EBSD: **a** EBSD band contrast map in which dark grey and light grey areas are austenite and ferrite, the green and purple are K–S and N–W interfaces and the red and blue lines are Σ3 and Σ9 CSL boundaries, respectively. Dashed yellow circles show examples of the formation of Σ9 boundaries at the intersection of Σ3 s. **b** Inverse pole figures constructed for the normal direction of the hot-rolled plate, showing the starting crystallographic texture. **c**–**e** Misorientation angle histograms for the austenite–austenite (**c**), austenite–ferrite (**d**) and ferrite–ferrite (**e**) boundaries.

Table 1 Plane and direction parallelism conditions and misorientation angle–axis pairs between FCC and BCC phases under different orientation relationships [21–25]

Orientation relationship	Parallelism	Minimum angle-axis pair
Kurdjumov–Sachs (K–S)	$\{111\}_{fcc}//\{110\}_{bcc}$	42.85°
	$<110>_{fcc}//<111>_{bcc}$	<0.968 0.178 0.178>
Greninger–Troiano (G–T)	$\{111\}_{fcc}//\{110\}_{bcc}$	44.23°
	$<123>_{fcc}//<133>_{bcc}$	<0.973 0.189 0.133>
Bain (B)	$\{100\}_{fcc}//\{100\}_{bcc}$	45°
	$<100>_{fcc}//<110>_{bcc}$	<1 0 0>
Pitsch (P)	$\{100\}_{fcc}//\{110\}_{bcc}$	45.98°
	$<110>_{fcc}//<111>_{bcc}$	<0.08 0.2 0.98>
Nishiyama–Wassermann (N–W)	$\{111\}_{fcc}//\{110\}_{bcc}$	45.98°
	$<112>_{fcc}//<110>_{bcc}$	<0.976 0.083 0.201>

cooling rather than being debris of pre-existing austenite not fully dissolved during the isothermal holding at 1370 °C. Such a lath- or needle-like morphology offers a minimum surface to volume energy ratio [26]. Most of the ferrite–ferrite boundaries were covered with allotriomorphic austenite particles. In addition, intragranular austenite particles with a variety of orientations were dispersed within the ferrite grains. Some $\Sigma3$ (60°/<111>) and $\Sigma9$ (38.9°/

<110>) austenite–austenite boundaries were observed in the microstructure, though the population of these boundaries ($\Sigma9$ in particular) was much lower than that under the rolled condition. The ferrite texture (Fig. 2b) in the heat-treated microstructure was similar to that in the hot-rolled condition, although it was slightly strengthened. Surprisingly, the austenite formed after heat treatment also displayed similar texture to that of the hot-rolled
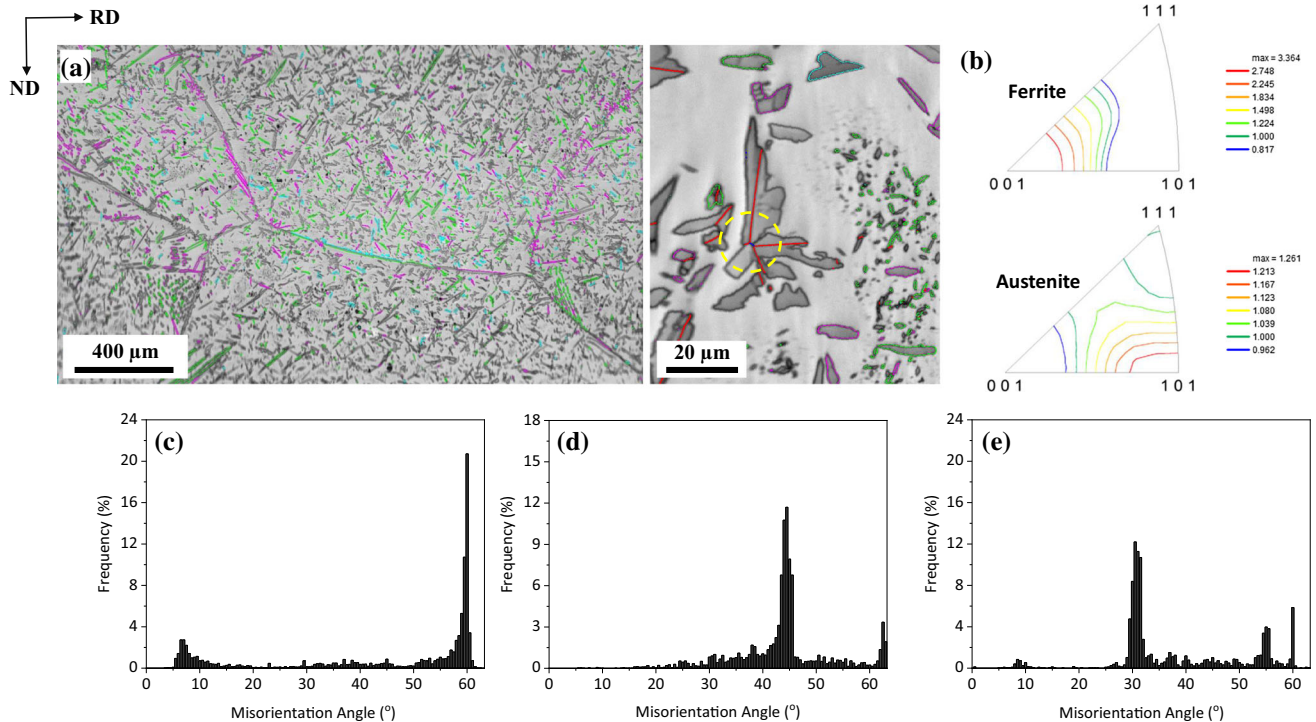

Figure 2 Characteristics of the steel after holding at 1370 °C for 40 min followed by water quenching obtained by EBSD: **a** EBSD band contrast map in which dark grey and light grey areas are austenite and ferrite; the green, purple and aqua lines are K–S, N–W and 54°/<9 4 12> interfaces, and the red and blue lines are $\Sigma3$ and $\Sigma9$ CSL boundaries, respectively. The dashed yellow circle shows an example of formation of $\Sigma9$ boundary at the intersection of $\Sigma3$ boundaries. **b** Inverse pole figures constructed for the normal direction of the original hot-rolled plate, showing the crystallographic texture after heat treatment. **c–e** Misorientation angle histograms for the austenite–austenite (**c**), austenite–ferrite (**d**) and ferrite–ferrite (**e**) boundaries.

material, showing a peak at <110>//ND (see Figs. 1b and 2b).

The misorientation angle distribution (Fig. 2c) for the austenite–austenite interfaces revealed peaks at the location of low-angle grain boundaries (∼ 5°) and at 60°. The misorientation angle distribution for austenite–ferrite interfaces, again, showed a pronounced peak at 42° to 46°, but with a secondary peak at ∼ 62° (Fig. 2d). The misorientation angle distribution of the ferrite–ferrite boundaries (Fig. 2e) showed peaks at ∼ 30°, 55° and 60°.

The plane character distribution for the main austenite–austenite boundaries (i.e., Σ3 and Σ9) exhibited a sharp anisotropy (Fig. 3). Σ3 boundaries mostly had the (111) plane orientation. Thus, such boundaries were of a pure twist character as the axis, <111>, was parallel to the plane normal, [111]. The above characteristics of FCC Σ3 boundaries have been largely reported in different single-phase and multi-phase materials under different phase transformations [7, 27] and thermomechanical conditions [28–31]. In the case of Σ9 boundaries, multiple peaks appeared though they were all located in the tilt boundaries zone planes, where the misorientation axis, [110], and the plane normal are perpendicular.

More specifically, there were peaks at the $(\bar{2}\,21)//(\bar{2}\,21)$ and $(1\bar{1}\,4)//(1\bar{1}\,4)$ symmetric tilt boundaries.

In order to obtain insight into the orientation relationships of the austenite grains with respect to the ferrite (parent phase), the measured austenite orientations were plotted in pole figure form and superimposed onto the variants of the theoretical Bain, K–S, N–W and Pitsch ORs (Fig. 4). Although the measured austenite orientations were distributed almost everywhere on the pole figure, there was also a significant concentration of these orientations *on* the Bain circles of the common ORs (K–S, N–W and Pitsch), meaning that for some of the grains, the *exact* ORs were followed. It is well known that the common ORs observed in FCC/BCC transformations can be grouped around the three Bain circles with only a few degrees (2.41°–5.27°) of deviation from each other in orientation space [32]. During the FCC-to-BCC phase transformation, the K–S and N–W relationships are very frequently observed [32–34], while during precipitation, the K–S, N–W and Pitsch, as well as those in between these ORs, e.g. G–T and inverse G–T [32], are often observed. It is noted that, in this work, even the Bain relationship (centres of the Bain circles), which was rarely observed in austenite-to-

Figure 3 **a**, **b** Misorientation axis distribution for the 38.9° and 60° austenite/austenite boundaries. Grain boundary character distribution at a fixed misorientation of **c** 38.9°/[110] and **d** 60°/[111] plotted in the [001] stereographic projection. The colour scale values are in MRD. The squares and circle represent the position of symmetric tilt and pure twist boundaries, respectively.
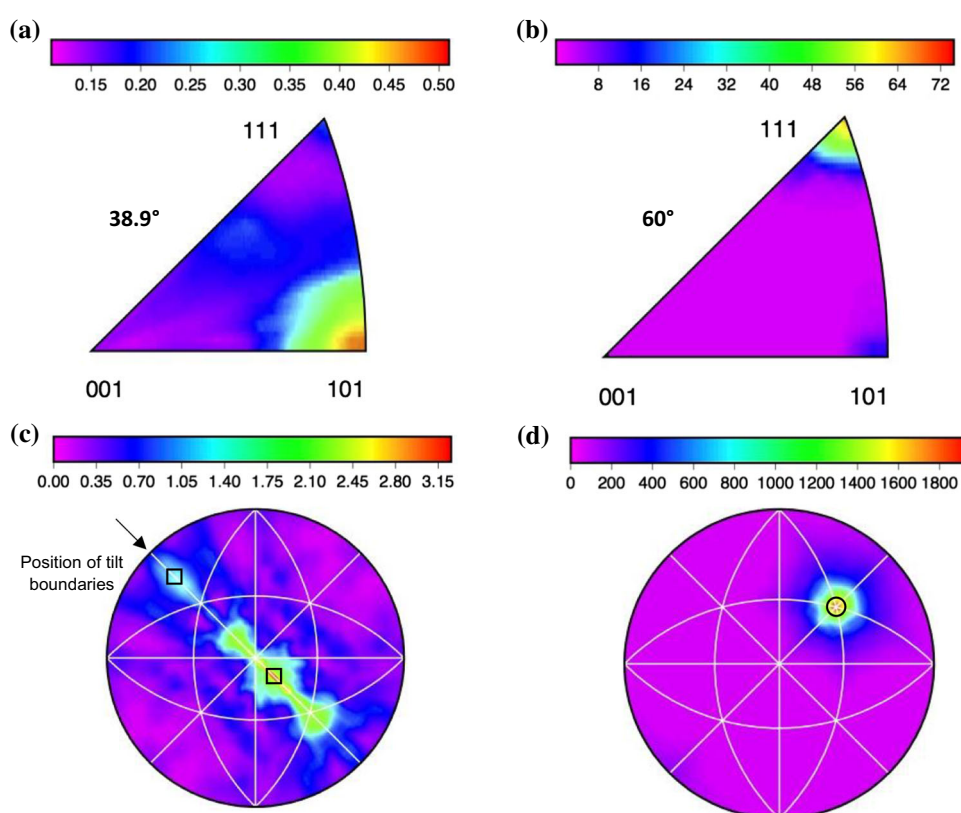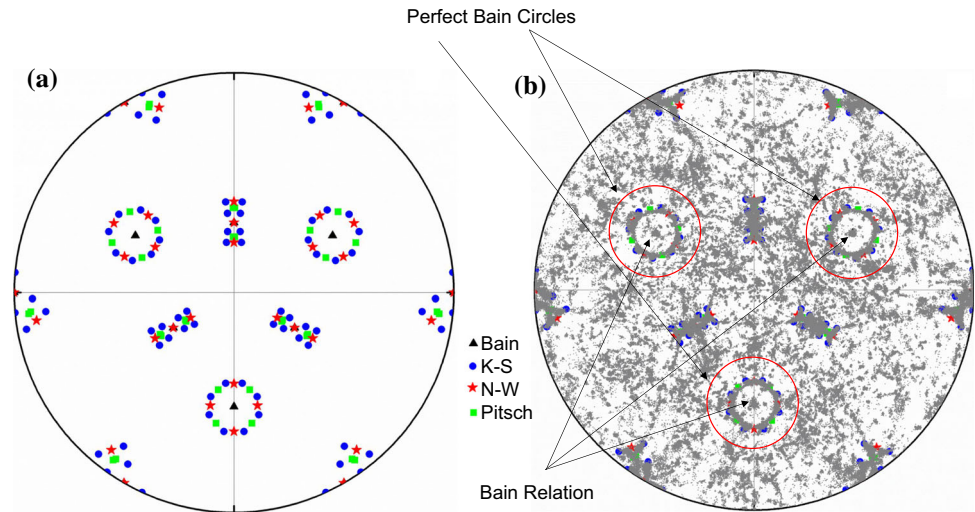
Figure 4 **a** Theoretical stereographic plot of $\{100\}_A$ poles for the Bain, K–S, N–W and Pitsch OR variants projected onto the $(111)_F$ plane. **b** Experimental $\{001\}$ pole figure of the austenite phase in the ferrite region.

martensite/bainite/Widmanstatten ferrite transformations [32–34], was also observed. However, it should be emphasized that, still a large amount of the austenite orientations did not follow any of the common orientation relationships between FCC and BCC.

Using a 2° tolerance for misorientation calculations, it was found that 8% and 7% of the austenite particles follow the K–S and N–W ORs, respectively. A more detailed microstructural observation revealed that there were some needle-like austenite particles with quite flat and almost parallel interfaces with ferrite (Fig. 2a), which did not correspond to any of the ORs summarized in Table 1. An individual analysis of their misorientation relative to the parent ferrite revealed that some of them followed a 54° misorientation angle along a <9 4 12> axis. To the best of our knowledge, this is the first time this OR between austenite and ferrite in a duplex stainless steel has been reported. It is to be noted that the population of these boundaries is not high enough to develop a distinctive peak around 54° in Fig. 2d.

Irrespective of lattice misorientation, the plane analysis of the austenite–ferrite interfaces showed peaks at $(111)_A//(110)_F$ (Fig. 5). A detailed analysis, however, revealed that for the austenite–ferrite interfaces, these phases tended to terminate on different habit planes at different lattice misorientations (Fig. 6). Austenite showed a peak at (111) plane for both K–S and N–W ORs, although the intensity of the peak in (111) was higher for the K–S than the N–W. For the 54°<9 4 12> misorientation, the peak, however, appeared at the (322) orientation spreading towards (111). On the other hand, ferrite terminated on the (110) plane for both the K–S and N–W lattice misorientations. Nevertheless, two separate peaks were observed at the (311) and (320) orientations for the 54°/[9 4 12] misorientation.

TEM analysis

Due to the small size of austenite particles, further investigation of the microstructures was conducted through TEM. As illustrated in Fig. 7a, the "edge-on" tilting of the ferrite/austenite interfaces revealed that they were mostly flat and devoid of steps. The TEM crystallographic analysis showed that these flat interfaces were generally aligned close to $\{110\}_F//\{111\}_A$ planes and the associated misorientations between the phases were typically closer to K–S than N–W, which is in line with the findings obtained through EBSD. This was also demonstrated by the oriented stereographic projections corresponding to ferrite and austenite, as shown in Fig. 7b, c, respectively. For the specific interphase boundaries shown in Fig. 7a, the orientation relationship between the phases deviated by about 3.9° and 8.2° from the K–S and N–W ORs, respectively. It is also seen from the above figure that there were frequent pile-ups of dislocations observed within austenite that, as expected, were located in {111} slip planes. STEM EDS analysis demonstrated that the chemical compositions of the ferrite and austenite were somewhat different, mainly showing partitioning of Ni and Mn towards austenite and Cr and Mo towards ferrite (Fig. 8).

Figure 5 Distributions of the austenite–ferrite interface boundary planes expressed in the **a** ferrite and **b** austenite crystal lattice frames. The colour scale represents MRD.
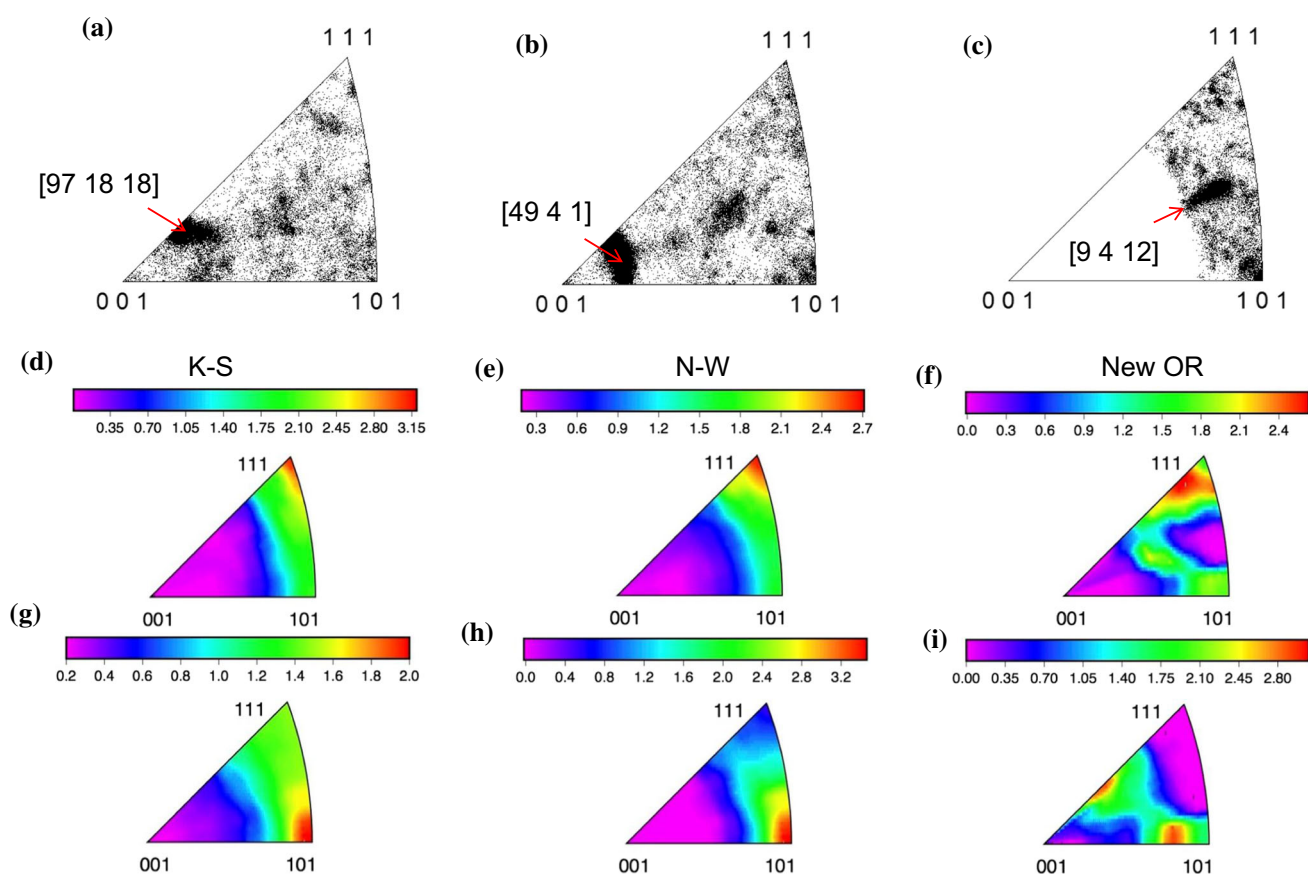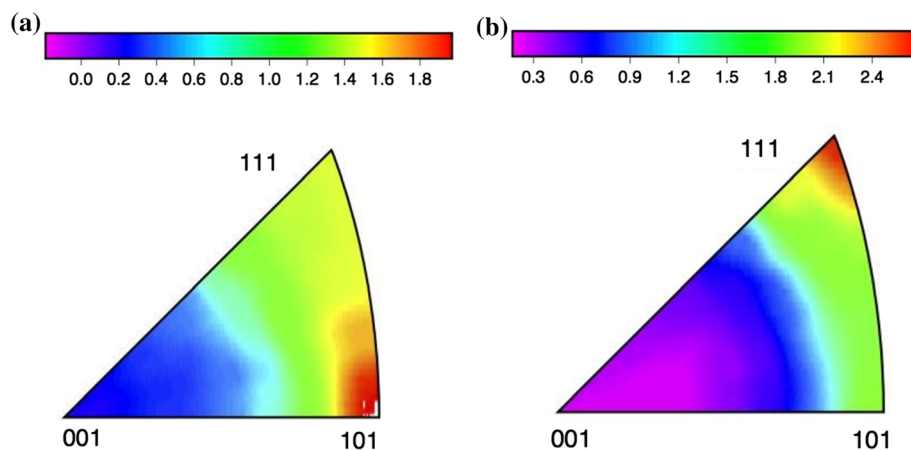

Figure 6 a–c Misorientation axis distribution for the **a** 43, **b** 46 and **c** 54° austenite–ferrite boundaries. **d–i** Distribution of the austenite–ferrite interface boundary planes, expressed in the **d–f** austenite and **g–i** ferrite crystal lattice frames, for different orientation relationships of **d, g** 42.85° <0.968 0.178 0.178> (K–S), **e, h** 45.98° <0.976 0.083 0.201> (N–W) and **f, i** 54°/<9 4 12>. The colour scale represents multiples of random distribution.

The TEM investigation also revealed the presence of misfit dislocations within the austenite/ferrite interfaces. The planar interphase boundaries characterised by the rational ORs, illustrated in Fig. 7, were typically observed to contain one dominant set of parallel, regularly spaced dislocations. In order to obtain an insight into the possible Burgers vector of these dislocations, foil tilting to several two-beam Bragg conditions around the $[001]_F$ zone axis was performed for a segment of the interphase boundary

Figure 7 a TEM bright-field micrograph of several austenite particles separated from the ferrite matrix by a planar interphase boundary in an "edge-on" orientation. Austenite and ferrite are labelled A and F, respectively. The arrows indicate dislocation pile-ups formed within austenite. **b** and **c** oriented stereographic projections corresponding to ferrite and austenite, respectively, documenting the near K–S OR between the two phases.
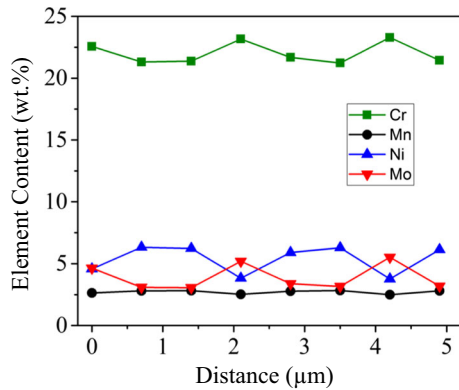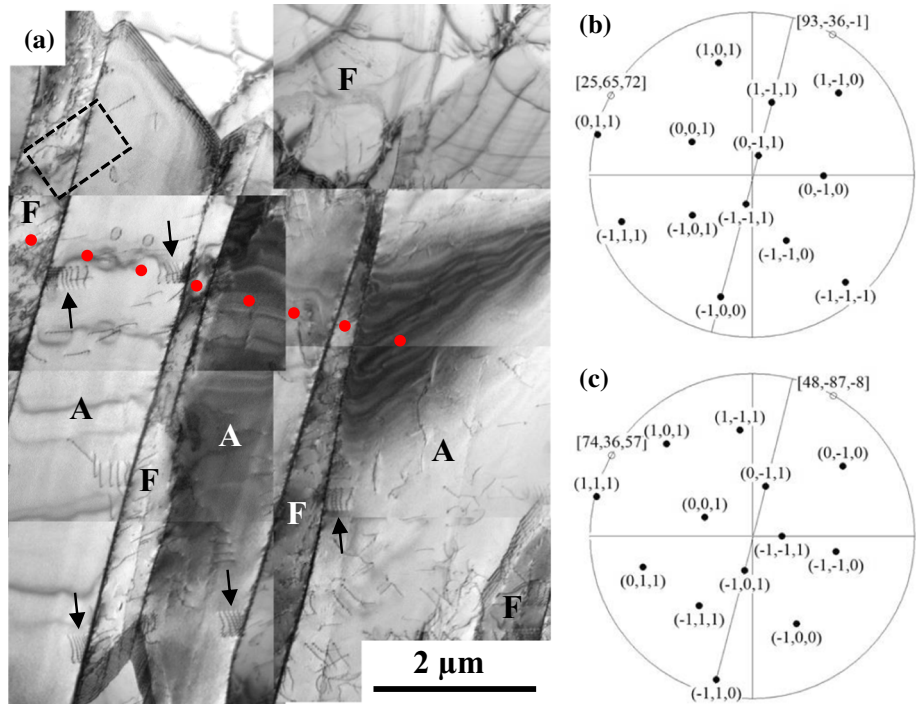

Figure 8 Variations in the content of the main alloying elements measured (from left to right) at the locations indicated by the red dots in Fig. 7a.

shown in Fig. 7a, and the g.b = 0 invisibility criterion [35] was applied, in which g and b are a reciprocal lattice vector corresponding to a strong Bragg reflection and a dislocation Burgers vector, respectively. It is seen from Fig. 9a–d that the set of dislocations was out of contrast when imaged using the $(1\bar{1}0)_F$ and in contrast when imaged using $(200)_F$, $(110)_F$ and $(020)_F$ reflections. From the above, it follows that the Burgers vector of the misfit dislocations could be either $a/2[111]_F$ or $a/2[\bar{1}\bar{1}1]_F$ that can be related through the Bain correspondence [35] to $a/2[101]_A$ and $a/2[\bar{1}01]_A$, respectively. Unfortunately,

the limited tilting capacity of the holder did not allow the possibility of reaching other prominent g vectors that would facilitate an unambiguous Burgers vector determination. In order to determine the true mean spacing of the misfit dislocations within the interphase boundary region shown in Fig. 10a, a corresponding oriented stereographic projection of ferrite was employed (Fig. 10b). The projection shows the inclination angle of 43.5° of a vector located in the interphase boundary plane and perpendicular to the dislocation lines. Through dividing a mean projected dislocation spacing of about 12.7 nm by the cosine of the above angle, a true dislocation spacing of about 17.5 nm was obtained.

Another interesting observation made through TEM was the occurrence of small protrusions appearing on the edge/face of some austenite particles. Some of these did not leave a sub-boundary behind and formed a finger-like austenite morphology (Fig. 11a), mostly resembling the protrusions that result from the instability mechanism [36]. In some other cases, the protruded austenite possessed a low-angle grain boundary with the substrate austenite grain (Fig. 11b). These were most likely the result of sympathetic nucleation of austenite on an existing austenite particle [37].

Figure 9 TEM two-beam bright-field micrographs of the ferrite/austenite interface section indicated by the small rectangle in the top-left corner of Fig. 7a. The diffraction **g** vectors used to generate these micrographs are $(1\bar{1}0)_F$ in **a**, $(200)_F$ in **b**, $(110)_F$ in **c** and $(020)_F$ in **d**. Austenite and ferrite are labelled A and F, respectively.
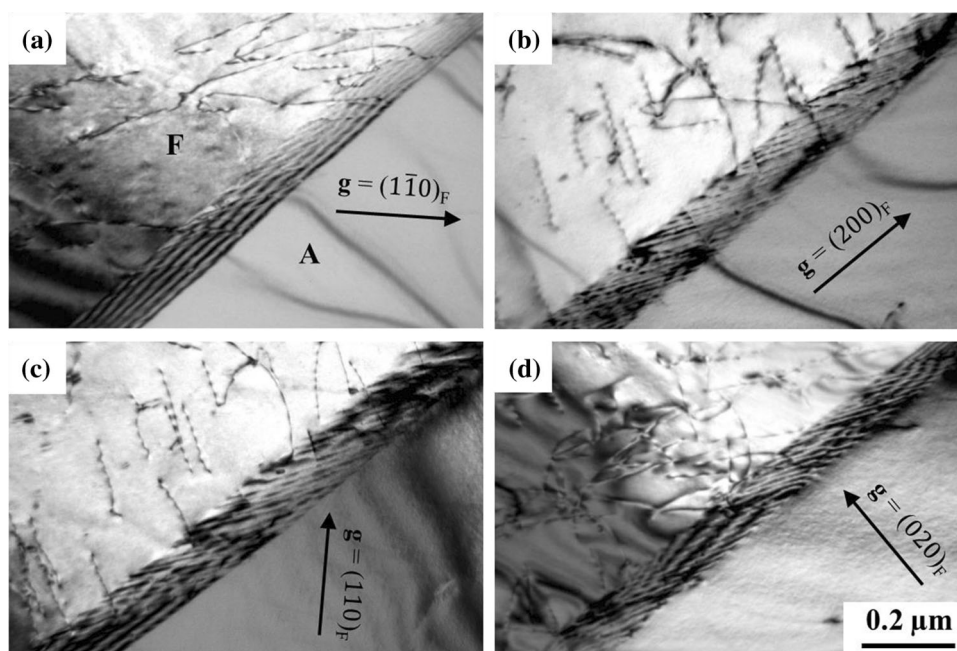
Discussion

Texture

The strengthening of the texture in ferrite during reheating and water-quenching can be ascribed to the dominance of the rotated cube component. It has been shown that this texture component possesses a strong tendency to recover rather than to recrystallize and it would be strengthened during high-temperature annealing [38]. Hutchinson et al. [39] also observed a texture sharpening in ferrite once it undergoes normal grain growth. In fact, annealing prior to transformation leads to pronounced recovery due to the high stacking fault energy of the ferrite.

The similarity of austenite textures between the hot-rolled and heat-treated conditions can be interpreted in different ways. This might be due to the incomplete dissolution of austenite at 1370 °C, where the austenite particles in the quenched conditions are the remnants of those present before the reheating or the result of the coarsening of the remnant austenite particles. This, however, does not seem to be very likely, considering the coarse size of the ferrite grains after heat treatment. According to Ref. [40], grain growth during annealing of duplex stainless steel is restricted due to the mutual constraint of ferrite and austenite on each other. The significant grain growth seen in Fig. 2a therefore suggests that the initial austenite was mostly dissolved during the reheating

treatment and the austenite particles were largely formed during quenching. Note that because of the relatively high nitrogen content of the experimental alloy, the formation of austenite at such high cooling rates is not very surprising [41].

The rotated cube component, which is the main texture component of ferrite [9], can result in Brass ({011}<211>) component in austenite if a K–S or N–W OR is dominant. This might be the reason why the <110>//ND fibre comprised the sharpest peak in the inverse pole figure of the transformed austenite. It should be noted, though, that austenite also showed other (non-<110>) texture components, which actually resembled the initial austenite texture. In fact, the austenite texture was qualitatively reproduced after an austenite-to-ferrite-to-austenite transformation cycle. This could be mostly attributed to a "texture memory effect", implying that the final austenite texture following the austenite → ferrite → austenite transformation was inherited from the texture of the primary austenite through a preferential orientation transformation. Such phenomenon has been previously reported for austenite → ferrite → austenite as well as ferrite → austenite → ferrite transformations [7, 42, 43].

Microstructure

The ferrite-to-austenite phase transformation in this study occurs in a very short time period, and the
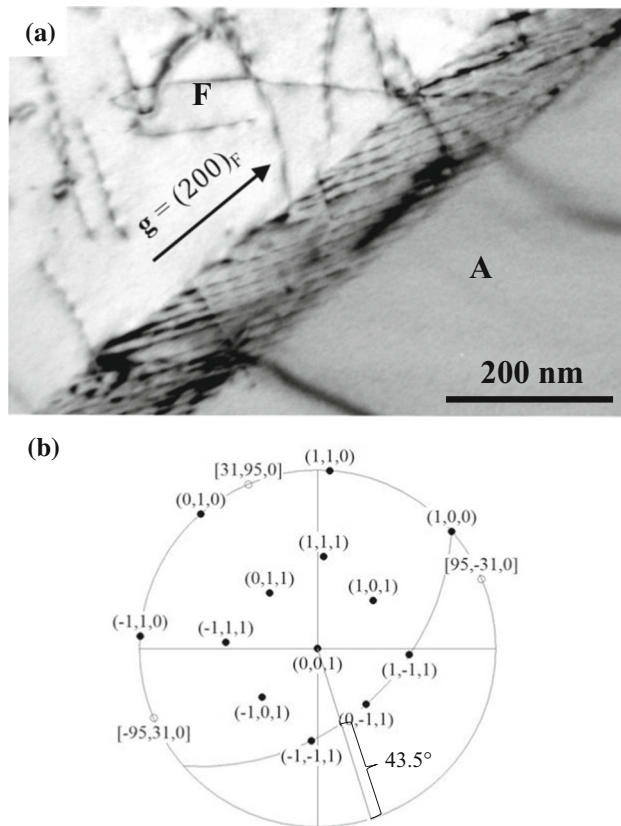
(a)

(b)

Figure 10 a Enlarged part of the interphase boundary segment from Fig. 9b, obtained using the diffraction vector $\mathbf{g} = (200)_F$, used for the determination of the corresponding dislocation spacing. Austenite and ferrite are labelled A and F, respectively. **b** Oriented stereographic projection of ferrite, showing the inclination angle of 43.5° of a vector located in the interphase boundary plane and being perpendicular to the dislocation lines. The above angle has been used to calculate the actual interphase boundary dislocation spacing. See the text for details.

intragranular austenite particles exhibit a lath-like morphology, similar to the products of displacive transformations. The detailed STEM/EDS analysis of the microstructures, however, shows that the chemical compositions of ferrite and austenite are different, mainly showing partitioning of Ni and Mn towards austenite and Cr and Mo towards ferrite (Fig. 8). This appears to be consistent with the "diffusion-limited" displacive mechanism [44], where the phase transformation leads to the (1) formation of regions enriched in Ni and Mn and depleted of Cr and Mo inside ferrite grains, and (2) displacive transformation of ferrite to austenite at these locations. This is also in line with the mechanism of lath austenite formation suggested in [45], where shear was considered

dominant, but also accompanied by prior or simultaneous diffusional elemental redistribution. The presence of dislocations in austenite might, therefore, originate from the shear component of transformation as well as from the residual stresses induced by fast cooling.

The size of the austenite particles formed in this work is significantly smaller than those formed during furnace or air cooling of ferrite in the same alloy [7]. This is due to a higher density of nuclei formed under stronger undercooling and limited growth due to suppressed diffusion of substitutional atoms. Another factor impacting the size of austenite particles might be related to the kinetics of dislocation displacement that occurs during lattice change (distortion). At low transformation temperatures, these dislocations will rarely be annihilated. These dislocations produce a back-stress field at the front of the austenite laths that, in turn, impedes the transformation (growth) [44].

Austenite–ferrite boundaries

Many austenite particles had a random orientation relationship with the parent ferrite grain (outside the Bain region). The reason behind this phenomenon could be different for intergranular and intragranular austenite particles. Adachi et al. [46] have demonstrated that during the austenite-to-ferrite transformation, a daughter ferrite crystal can simultaneously fulfil the KS OR with respect to both the adjacent parent austenite grains (i.e., it can hold a dual KS OR) only for specific orientation relationships between the parent grains. This will not occur at boundaries that do not have this special orientation relationship. Because the majority of the parent ferrite–ferrite boundaries in the current work do not have a special orientation relationship, not all the austenite particles will have the KS or NW OR. Even if the daughter austenite particles nucleated at the grain boundaries or triple junctions hold the K–S OR or N–W OR with one of the grains, they will have a high-energy incoherent interface having no special OR with the other grain. It has also been reported that the chances of obtaining dual ORs are even more limited when transformations take place at high undercooling (fast cooling rates) [47]. Such a deviation from rational ORs has also been reported by King and Bell [48], where it was ascribed to the selective growth of austenite. It has been proposed that, although a

Figure 11 a TEM bright-field micrograph of an austenite particle surrounded by the ferrite matrix. The arrows indicate dislocation pile-ups formed within austenite. **b** TEM bright-field micrograph showing an austenite particle, indicated by the arrow, likely formed through sympathetic nucleation on the austenite/ferrite interface. Numbers 1 and 2 denote the locations used for the orientation determination. See the text for details. In **a** and **b**, austenite and ferrite are labelled A and F, respectively.
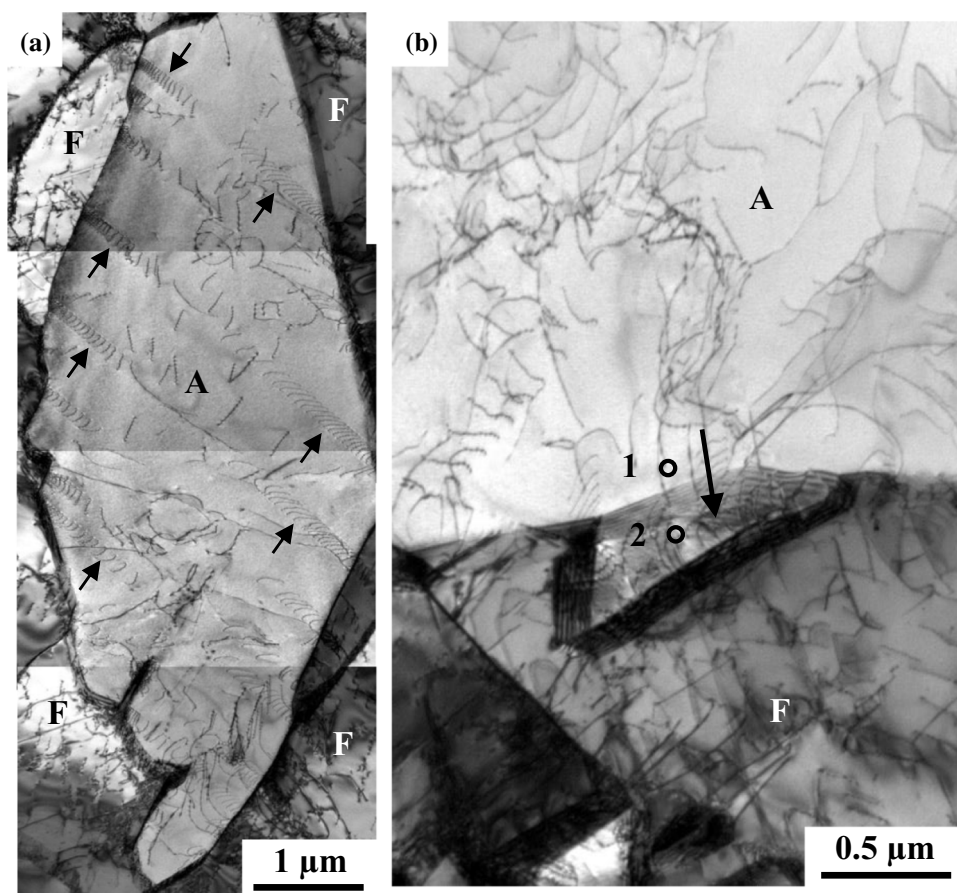
rational OR might minimize the activation energy, the growth will be favoured along the irrational interfaces [48]. Therefore, even for the austenite particles that have experienced homogenous nucleation, a large fraction of interfaces with ferrite have a random misorientation.

The orientation of intragranular austenite with respect to the parent ferrite is determined by the cooling rate, which affects both the transformation driving force and the availability of nitrides that might serve as heterogeneous nucleation sites for austenite [49]. Karlsson and Börjesson [50] have suggested that any change in the cooling rate and composition that lowers the transformation temperature would make the OR between austenite and ferrite more random. This is, however, in contrast to our previous work where it was shown that the population of rational boundaries rose as the transformation rate increased [7]. This makes the role of nitrides more important in the current work. Due to the supersaturation of nitrogen in ferrite, there is a high chance of the formation of intragranular austenite on nitrides having a random OR with the

ferrite matrix. Hexagonal Cr_2N particles can form during water quenching due to supersaturation of nitrogen in ferrite. The existence of these particles in the microstructure has been verified through high-resolution EBSD and detailed TEM analysis of the microstructure (Fig. 12). The above arguments might explain why the population of rational interfaces in this study was lower than those reported in a previous study on air-cooled duplex stainless steel [7].

It is to be noted that there are two possible reasons for the formation of austenite adjacent to Cr_2N particles. It could be a result of the well-known minimization of interface energy once nucleation occurs on an existing interface [51]. Another possible mechanism would be the formation of austenite in regions very close to Cr_2N particles due to some possible solute depletion therein. In order to investigate this, the formation of Cr_2N inside ferrite upon cooling and the solute distribution near the Cr_2N–ferrite interface was simulated using the DICTRA software with the MOBFE4 mobility database. The cooling process started from 1350 to 600 °C with a constant cooling rate of 250 °C/s. A local equilibrium
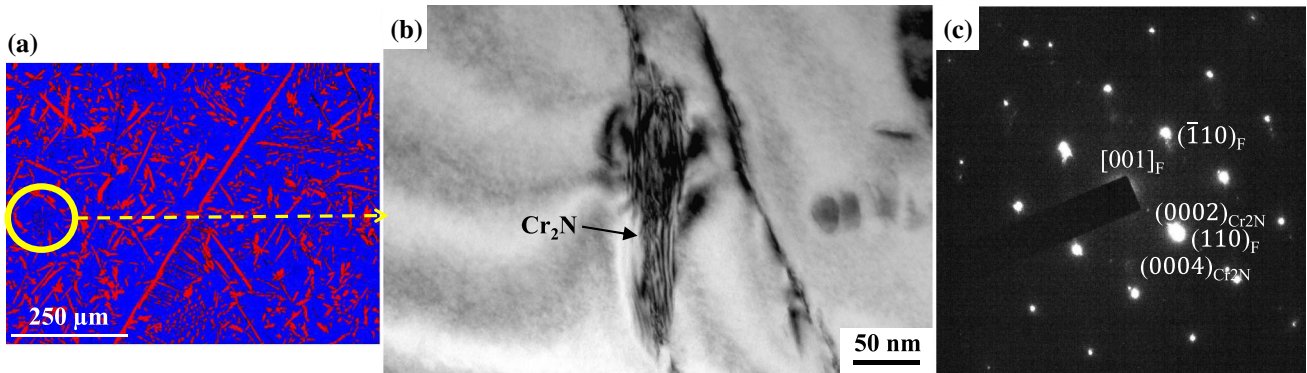
Figure 12 a EBSD image indicating regions containing small particles. **b** TEM bright-field micrograph of a Cr_2N particle embedded within the ferrite matrix. **c** SAD pattern corresponding to the [001] ferrite zone axis and containing Cr_2N reflections consistent with the Burgers orientation relationship.

condition was assumed at the moving interface. The simulations were performed considering a cylindrical geometry, with the Cr_2N particle embedded in the centre of ferrite whose grain size being assumed to be 100 μm. Five main chemical elements (Fe, C, N, Cr, Ni) were considered to simplify the simulation. The results show a depletion of N and Cr near the interface. The degree of such depletion increases during cooling (Fig. 13a, b). The local driving force of the ferrite-to-austenite transformation was evaluated for regions just adjacent to the interface (depletion zones) and regions far away from the interface, using the Thermo-Calc software with the TCFE9 database. It was observed that the austenite formation driving force is actually reduced in areas near the interface (Fig. 13c), which is due to the depletion of N. This

suggests the solute depletion is unlikely to be the reason for the observed austenite formation adjacent to the Cr_2N particles.

The dominance of the K–S over the N–W OR is another interesting observation for the current reheated and rapidly quenched duplex stainless steel. There might by several reasons behind this phenomenon. It has been reported that the coherent elastic energy of the austenite–ferrite interface increases with increasing the interatomic distance for the two phases in a parallel direction [52]. As shown in Table 1, the direction parallelism between these phases is $<110>_A//<111>_F$ and $<112>_A//<110>_F$ for K–S and N–W ORs, respectively, which means the interatomic distances for the K–S $(\frac{\sqrt{2}}{\sqrt{3}}\frac{L_A}{L_F})$ is lower than
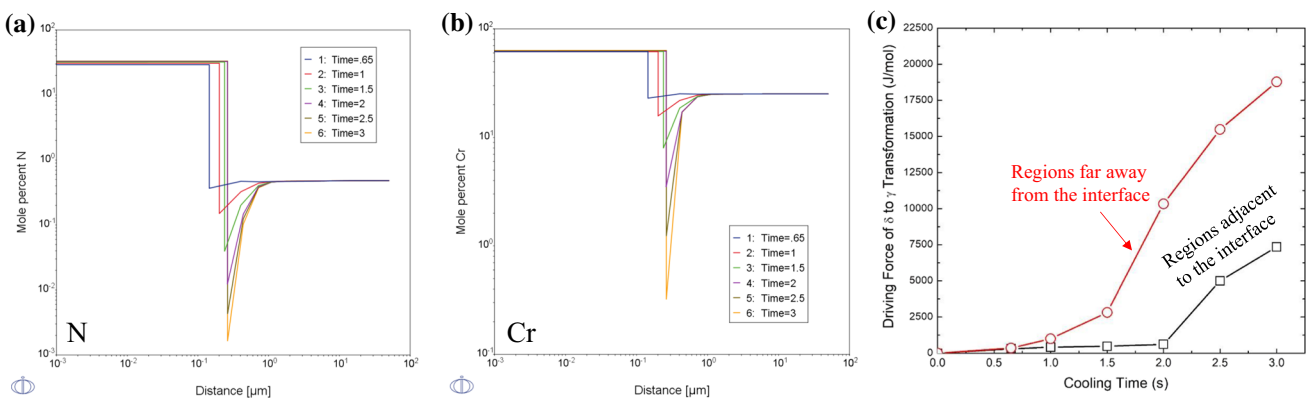

Figure 13 The simulated chemical composition at the interface of ferrite and Cr2N showing a depletion of **a** N and **b** Cr near the interface using the DICTRA software with the MOBFE4 mobility database. **c** The local driving force of ferrite-to-austenite transformation for regions just adjacent to the interface (depletion zones) and regions far away from the interface, using the Thermo-Calc software with the TCFE9 database.

that in the N–W ($\frac{\sqrt{3}}{2}\frac{L_A}{L_F}$). This can also justify the more pronounced dominance of the K–S over the N–W at lower cooling rates reported in Ref. [7] compared to this work, as $\frac{L_A}{L_F}$ increases with an increase in the transformation temperature. It has also been revealed by Nagano and Enomoto [53] that during the homogeneous nucleation of ferrite in austenite, a K–S orientation will minimize the interphase boundary energy compared to an N–W orientation. Moreover, the preference of the K–S over the N–W can be attributed to the enhanced atom matching along or near the invariant line direction for the former OR [26].

For both the K–S and N–W ORs, austenite and ferrite tend to terminate on (111) and (110) planes, respectively. This is in line with the theoretical plane parallelism suggested for these lattice correspondences (Table 1). The above planes have been reported to have the minimum energy using both atomistic models [54] and experimental measurements [28]. In the case of the new OR suggested in the present work (54°/<9 4 12>), interestingly, austenite tends to terminate on (322) planes and ferrite on (311) and (320) planes. A detailed study of the reasons behind this remains to be clarified and requires further work. The observed largely planar character of the austenite–ferrite interfaces (Fig. 7) appears to imply that the transformation is most likely interface controlled rather than diffusion controlled, as the majority of the free energy attending the transformation has been dissipated by interfacial processes (BCC to FCC rearrangement) rather than by bulk solute diffusion. It has been widely accepted that the transformation strain is generally accommodated by interfacial dislocations, which causes a loss in the coherency of the interface [51]. Indeed, there has been one set of parallel, equally spaced dislocations observed within the planar interfaces following the KS OR characteristics (see Figs. 9, 10).

Austenite–austenite boundaries

The austenite–austenite boundaries within the intragranular austenite particles might have been formed for three main reasons. They might be the result of (1) (multiple) twinning of grains (Σ3 and Σ9), (2) impingement of grains with distinct orientations during growth, developing an intervariant boundary and (3) sympathetic nucleation where one grain forms on the edge or face of another grain leaving behind a low-angle grain boundary.

It has been reported that minimization of the overall grain boundary energy is the main driving force for the formation of Σ3 s [7]. In the case of austenite forming inside ferrite, the twin boundaries also help the growth of austenite by providing an easy growth mechanism, similar to the spiral growth mechanism [51]. The population of CSL boundaries (in particular Σ9 s) in the studied microstructure (water-quenched) is considerably lower than the air-cooled and furnace-cooled microstructures reported in previous studies [7]. This is mostly due to a kinetic effect. As shown in another investigation [7], the population of twins decreases as the transformation period decreases. The lower population of Σ9 boundaries is, therefore, due to the limited growth of austenite particles during transformation, as the formation of Σ9 boundaries is mainly the result of the impingement of two Σ3 s. There are several ideas about how and why annealing twins are formed. Based on one of these models suggested by Fullman and Fisher [55], which has been recently verified through a 3D EBSD analysis [56], a decrease in the free energy of the grain boundaries is the main driving force for the formation of Σ3 s. In particular, a coherent twin boundary would decrease the energy of the boundary most significantly. This is the reason why most of the Σ3 s are of (111) twist boundaries, which are the minimum energy Σ3 boundaries. The twist character of the Σ3 boundaries places a geometric constraint on the limited number of observed Σ9 boundaries, forcing them to have a tilt character, as described in [29].

Some of the austenite/austenite boundaries in the microstructure form as a result of the impingement of different grains while they grow. Nolze [57] has calculated the misorientation angle/axis resulting from impingement of different K–S and N–W variants during the ferrite-to-austenite transformation. The volume fraction of these boundaries in the present study was, however, very limited due to restricted growth of different austenite particles. It has been previously shown that if austenite particles impinge, irrespective of their misorientation, they tend to terminate on (111) planes [7].

The low-angle austenite–austenite boundaries (mostly seen only through TEM because they have misorientation angles less than the typical resolution of EBSD—see Fig. 11b) are the results of sympathetic

nucleation. It has been reported [58] that the activation energy for sympathetic nucleation is comparable to homogenous and heterogeneous second phase-on-matrix nucleation because this causes the matrix-second phase boundary to be replaced by a low-energy second phase–second phase interface. As reported in [59], the formed boundaries always have a low angle. It is, however, to be noted that the nucleation energy would be minimized if the sympathetically nucleated austenite had exactly the same orientation with its parent grain [60]. The formation of low-angle boundaries during sympathetic nucleation is rationalized as follows. The sympathetic nucleation frequently takes place at semi-coherent interphase boundaries between growth ledges. These interfaces are of low energy and mobility. New grains that are sympathetically nucleated at the misfit dislocations in semi-coherent facets tend to show some distance from the misfit dislocations to increase the nuclei coherency [60]. The shear strain associated with the transformation may also play an important role in sympathetic nucleation. It has been reported that sympathetic nucleation will be encouraged when a strain component parallel to a plate face can neutralize the strain generated by the adjacent plate [61].

Conclusions

In the current work, the ferrite-to-austenite phase transformation during water quenching of a duplex stainless steel from the ferritic region was studied. The main findings are as follows.

1. The microstructure of the studied duplex stainless steel after heating to 1370 °C followed by water quenching consisted of coarse ferrite grains and fine needle-like austenite particles. The most likely phase transformation mechanism is a "diffusion-limited" displacive mechanism where shear is dominant, but also accompanied by prior or simultaneous diffusional elemental redistribution.
2. The ferrite texture in the heat-treated microstructure was similar to that in the as-received condition; it was only slightly strengthened. Austenite formed after heat treatment displayed a similar texture to that of the as-received material, which was mainly attributed to the "texture memory effect". The misorientation angle distribution for austenite–ferrite showed a pronounced peak at the misorientation angle range of 42° to 46° corresponding to main theoretical FCC-BCC orientation relationships (Bain, K–S, N–W and Pitsch).
3. Interphase boundaries of K–S and N–W ORs terminated on $(111)_A//(110)_F$ planes which are the preferred planes based on both energy and crystallography considerations. The $54°/<9\ 4\ 12>$ interfaces terminated on $(322)_A$, and $(311)_F$ and $(320)_F$ planes.
4. The high undercooling associated with the fast cooling rate resulted in a considerable deviation from the rational ORs. This could be mostly due to the formation of intragranular austenite particles on Cr_2N, which will make them have a random OR with the ferrite matrix.
5. The planar interphase boundaries characterised by the rational ORs were typically observed to contain one dominant set of parallel, regularly spaced dislocations. A true dislocation spacing of about 17.5 nm was obtained for one of the interphase boundaries.
6. TEM analysis indicted the occurrence of small protrusions appearing on edges/faces of some austenite particles. Some of these did not leave a sub-boundary behind and formed a finger-like austenite morphology presumably resulting from the instability mechanism. In some other cases, the protruded austenite possessed a low-angle grain boundary with a substrate austenite grain, most likely being the result of sympathetic nucleation of austenite on an existing austenite particle.

Compliance with ethical standards

Conflict of interest   The authors declare no conflict of interest.

References

[1] Schuh CA, Kumar M, King WE (2003) Analysis of grain boundary networks and their evolution during grain boundary engineering. Acta Mater 51:687–700

[2] Randle V (2004) Twinning-related grain boundary engineering. Acta Mater 52:4067–4081

[3] Watanabe T (2011) Grain boundary engineering: historical perspective and future prospects. J Mater Sci 46:4095–4115. https://doi.org/10.1007/s10853-011-5393-z

[4] Farabi E, Hodgson PD, Rohrer GS, Beladi H (2018) Five-parameter intervariant boundary characterization of martensite in commercially pure titanium. Acta Mater 154:147–160

[5] Beladi H, Rohrer GS (2017) The role of thermomechanical routes on the distribution of grain boundary and interface plane orientations in transformed microstructures. Metal. Mater. Trans. A 48:2781–2790

[6] Gunn RN (1997) Duplex Stainless Steels: Microstructure. Woodhead Publishing, Cambridge, Properties and Applications

[7] Haghdadi N, Cizek P, Hodgson PD, Tari V, Rohrer GS, Beladi H (2018) Effect of ferrite-to-austenite phase transformation path on the interface crystallographic character distributions in a duplex stainless steel. Acta Mater 145:196–209

[8] Haghdadi N, Abou-Ras D, Cizek P, Hodgson PD, Rollett AD, Beladi H (2017) Austenite–ferrite interface crystallography dependence of sigma phase precipitation using the five-parameter characterization approach. Mater. Let. 196:264–268

[9] Haghdadi N, Cizek P, Hodgson PD, Beladi H (2019) Microstructure dependence of impact toughness in duplex stainless steels. Mater Sci Eng A 745:369–378

[10] Haghdadi N, Laleh M, Kosari A, Moayed MH, Cizek P, Hodgson PD, Beladi H (2019) The effect of phase transformation route on the intergranular corrosion susceptibility of 2205 duplex stainless steel. Mater. Let. 238:26–30

[11] Haghdadi N, Cizek P, Beladi H, Hodgson PD (2017) Dynamic restoration processes in a 23Cr-6Ni-3Mo duplex stainless steel: Effect of austenite morphology and interface characteristics. Metal. Mater. Trans. A 48:4803–4820

[12] Pinol-Juez A, Iza-Mendia A, Gutierrez I (2000) δ/γ interface boundary sliding as a mechanism for strain accommodation during hot deformation in a duplex stainless steel. Metal Mater Trans A 31(6):1671–1677

[13] Qiu D, Zhan W-Z (2007) A TEM study of the crystallography of austenite precipitates in a duplex stainless steel. Acta Mater 55:6754–6764

[14] Jiao H, Aindow M, Pond RC (2003) Precipitate orientation relationships and interfacial structures in duplex stainless steel Zeron-100. Philos. Mag. 83:1867–1887

[15] Ameyama K, Weatherly GC, Aust KT (1992) A study of grain boundary nucleated widmanstätten precipitates in a two-phase stainless steel. Acta Metal. Mater. 40:1835–1846

[16] Rohrer GS, Saylor DM, El Dasher B, Adams BL, Rollett AD, Wynblatt P (2004) The distribution of internal interfaces in polycrystals. Z Metallkd 95:197–214

[17] Haghdadi N, Cizek P, Beladi H, Hodgson PD (2017) A novel high-strain-rate ferrite dynamic softening mechanism facilitated by the interphase in the austenite/ferrite microstructure. Acta Mater 126:44–57

[18] Wright SI, Larsen RJ (2002) Extracting twins from orientation imaging microscopy scan data. J. Micros. 205:245–252

[19] Raabe D, Ylitalo M (1996) Experimental investigation of the transformation texture in hot rolled ferritic stainless steel using single orientation determination. Metal. Mater. Trans. 27:49–57

[20] Kang JY, Bacroix B, Réglé H, Oh KH, Lee HC (2007) Effect of deformation mode and grain orientation on misorientation development in a body-centered cubic steel. Acta Mater 55:4935–4946

[21] Kurdjumov G, Sachs G (1930) Over the mechanisms of steel hardening. Z. Phys. 64:325–343

[22] Nishiyama Z (1934–1935) X-ray investigation of the mechanism of the transformation from face centered cubic lattice to body centered cubic. Sci Rep Res Inst Tohoku Univ. 23:637–638

[23] Greninger AB, Troiano AR (1949) The mechanism of martensite formation. JSME Trans. 185:590–598

[24] Pitsch W (1962) Der orientierung szusammenhang zwischen zementit und austenite. Acta Metall 10:897–900

[25] Bain EC (1924) The nature of martensite. Trans. AIME 70:25–47

[26] Weatherly GC, Zhang W-Z (1994) The invariant line and precipitate morphology in Fcc-Bcc systems. Metal. Mater. Trans. A 25:1865–1874

[27] Haghdadi N, Cizek P, Hodgson PD, Tari V, Rohrer GS, Beladi H (2018) Five-parameter crystallographic characteristics of the interfaces formed during ferrite to austenite transformation in a duplex stainless steel. Phil Mag 98:1284–1306

[28] Beladi H, Nuhfer NT, Rohrer GS (2014) The five-parameter grain boundary character and energy distributions of a fully austenitic high-manganese steel using three dimensional data. Acta Mater 70:281–289

[29] Rohrer GS, Randle V, Kim CS, Hu Y (2006) Changes in the five-parameter grain boundary character distribution in α-

brass brought about by iterative thermomechanical processing. Acta Mater 54:4489–4502

[30] Li J, Dillon SJ, Rohrer GS (2009) Relative grain boundary area and energy distributions in nickel. Acta Mater 57:4304–4311

[31] Randle V, Rohrer GS, Miller HM, Coleman M, Owen GT (2008) Five-parameter grain boundary distribution of commercially grain boundary engineered nickel and copper. Acta Mater 56:2363–2373

[32] He Y, Godet S, Jonas JJ (2006) Observations of the Gibeon meteorite and the inverse Greninger–Troiano orientation relationship. J. App. Crystal. 39:72–81

[33] He Y, Godet S, Jacques PJ, Jonas JJ (2006) Crystallographic relations between face-and body-centred cubic crystals formed under near-equilibrium conditions: observations from the Gibeon meteorite. Acta Mater 54:1323–1334

[34] He Y (2005) Grain-scale characterization of FCC/BCC correspondence relations and variant selection, Doctoral Thesis, McGill University, Canada

[35] Williams DB, Carter CB (2009) Transmission Electron Microscopy—a Textbook for Materials Science. Springer, New York

[36] Townsend RD, Kirkaldy JS (1968) Widmanstatten ferrite formation in Fe-C alloys. Trans. ASM 61:605–619

[37] Chen CY, Yen HW, Yang JR (2007) Sympathetic nucleation of austenite in a Fe–22Cr–5Ni duplex stainless steel. Scripta Mater 56:673–676

[38] Badji R, Bacroix B, Bouabdallah M (2011) Texture, Microstructure and anisotropic properties in annealed 2205 duplex stainless steel welds. Mater. Charac. 62:833–843

[39] Hutchinson WB, Ryde L, Bate PS (2005) Transformation textures in steels. Mater Sci Forum 495:1141–1150

[40] Zaid M, Bhattacharjee PP (2014) Electron backscatter diffraction study of deformation and recrystallization textures of individual phases in a cross-rolled duplex steel. Mater. Charac. 96:263–272

[41] Muthupandi V, Srinivasan PB, Seshadri SK, Sundaresan S (2003) Effect of weld metal chemistry and heat input on the structure and properties of duplex stainless steel welds. Mater Sci Eng A 358:9–16

[42] Lischewski I, Gottstein G (2005) Orientation relationship during partial α-γ-phase transformation in microalloyed steels. Mater Sci Forum 495–497:447–452

[43] Brückner G, Gottstein G (2001) Transformation textures during diffusional $\alpha \rightarrow \gamma \rightarrow \alpha$ phase transformations in ferritic steels. ISIJ Int 41:468–477

[44] Christian JW (1994) Crystallographic theories, interface structures, and transformation mechanisms. Metal. Mater. Trans. A 25:1821–1839

[45] Ohmori Y, Nakai K, Ohtsubo H, Isshiki Y (1995) Mechanism of widmanstätten austenite formation in a δ/γ duplex phase stainless steel. ISIJ Int 35:969–975

[46] Adachi Y, Hakata K, Tsuzaki K (2005) Crystallographic analysis of grain boundary Bcc-precipitates in a Ni–Cr alloy by FESEM/EBSD and TEM/Kikuchi line methods. Mater. Sci. Eng. 412:252–263

[47] Kim DW, Qin RS, Bhadeshia HKDH (2009) Transformation texture of allotriomorphic ferrite in steel. Mater Sci Technol 25:892–895

[48] King AD, Bell T (1975) Crystallography of grain boundary proeutectoid ferrite. Metall Trans A 6:1429–1491

[49] Ramirez AJ, Lippold JC, Brandi SD (2003) The relationship between chromium nitride and secondary austenite precipitation in duplex stainless steels. Metal. Mater. Trans. A 34:1575–1597

[50] Karlsson L, Börjesson J (2014) Orientation relationships of intragranular austenite in duplex stainless steel weld metals. Sci. Technol. Weld. Join. 19:318–323

[51] Porter DA, Easterling KE (1992) Phase Transformation in Materials. Chapman & Hall, Boundary Row, London

[52] Gotoh Y, Uwaha M (1987) Geometrical Interpretation of the Interfacial Energy between bcc and fcc lattices and preferred orientation relationship of the epitaxy. Jap. J. App. Phys. 26:17–20

[53] Nagano T, Enomoto M (2006) Calculation of the interfacial energies between α and γ iron and equilibrium particle shape. Met. Mater. Trans. A 37:929–937

[54] Mackenzie JK, Moore AJW, Nicholas JF (1962) Bonds broken at atomically flat crystal surfaces-I: face-centred and body-centred cubic crystals. J. Phys. Chem. Solid. 23:185–196

[55] Fullman RL, Fisher JC (1951) Formation of annealing twins during grain growth. J Appl Phys 22:1350–1355

[56] Lin B, Jin Y, Hefferan CM, Li SF, Lind J, Suter RM, Bernacki M, Bozzolo N, Rollett AD, Rohrer GS (2015) Observation of annealing twin nucleation at triple lines in nickel during grain growth. Acta Mater 99:63–68

[57] Nolze G (2008) Irrational orientation relationship derived from rational orientation relationships using EBSD data. Crys. Res. Technol. J. Exp. Ind. Crystal. 43:61–73

[58] Menon ESK, Aaronson HI (1987) Overview no 57: morphology, crystallography and kinetics of sympathetic nucleation. Acta Metal 35:549–563

[59] Phelan D, Stanford N, Dippenaar R (2005) Widmanstätten ferrite nucleation in a low Carbon alloy. Mater Sci Eng A 407:127–134

[60] Aaronson HI, Russell KC (1983) In: Aaronson HI, Laughlin DE, Sekerka RF, Wayman CM (eds) Proceedings of an

international conference on solid-solid phase transformations. TMS-AIME, Warrendale, PA, (1983)

[61] Russell KC, Barnett DM, Altstetter CJ, Aaronson HI, Lee JK (1977) Strain energy interactions, the T_0 concept and sympathetic nucleation. Scr Metall 11:485–490

Publisher's Note Springer Nature remains neutral with regard to jurisdictional claims in published maps and institutional affiliations.